

UvA-DARE (Digital Academic Repository)

Adsorption equilibrium of nitrogen dioxide in porous materials

Matito-Martos, I.; Rahbari, A.; Martin-Calvo, A.; Dubbeldam, D.; Vlugt, T.J.H.; Calero, S.

DOI

[10.1039/c7cp08017d](https://doi.org/10.1039/c7cp08017d)

Publication date

2018

Document Version

Final published version

Published in

Physical Chemistry Chemical Physics

License

Article 25fa Dutch Copyright Act

[Link to publication](#)

Citation for published version (APA):

Matito-Martos, I., Rahbari, A., Martin-Calvo, A., Dubbeldam, D., Vlugt, T. J. H., & Calero, S. (2018). Adsorption equilibrium of nitrogen dioxide in porous materials. *Physical Chemistry Chemical Physics*, 20(6), 4189-4199. <https://doi.org/10.1039/c7cp08017d>

General rights

It is not permitted to download or to forward/distribute the text or part of it without the consent of the author(s) and/or copyright holder(s), other than for strictly personal, individual use, unless the work is under an open content license (like Creative Commons).

Disclaimer/Complaints regulations

If you believe that digital publication of certain material infringes any of your rights or (privacy) interests, please let the Library know, stating your reasons. In case of a legitimate complaint, the Library will make the material inaccessible and/or remove it from the website. Please Ask the Library: <https://uba.uva.nl/en/contact>, or a letter to: Library of the University of Amsterdam, Secretariat, Singel 425, 1012 WP Amsterdam, The Netherlands. You will be contacted as soon as possible.



Cite this: *Phys. Chem. Chem. Phys.*,
2018, 20, 4189

Adsorption equilibrium of nitrogen dioxide in porous materials†

I. Matito-Martos,^a A. Rahbari,^b A. Martin-Calvo,^c D. Dubbeldam,^d
T. J. H. Vlugt^b and S. Calero^{*a}

The effect of confinement on the equilibrium reactive system containing nitrogen dioxide and dinitrogen tetroxide is studied by molecular simulation and the reactive Monte Carlo (RxMC) approach. The bulk-phase reaction was successfully reproduced and five all-silica zeolites (*i.e.* FAU, FER, MFI, MOR, and TON) with different topologies were selected to study their adoption behavior. Dinitrogen tetroxide showed a stronger affinity than nitrogen dioxide in all the zeolites due to size effects, but exclusive adsorption sites in MOR allowed the adsorption of nitrogen dioxide with no competition at these sites. From the study of the adsorption isotherms and isobars of the reacting mixture, confinement enhanced the formation of dimers over the full range of pressure and temperature, finding the largest deviations from bulk fractions at low temperature and high pressure. The channel size and shape of the zeolite have a noticeable influence on the dinitrogen tetroxide formation, being more important in MFI, closely followed by TON and MOR, and finally FER and FAU. Preferential adsorption sites in MOR lead to an unusually strong selective adsorption towards nitrogen dioxide, demonstrating that the topological structure has a crucial influence on the composition of the mixture and must be carefully considered in systems containing nitrogen dioxide.

Received 29th November 2017,
Accepted 18th December 2017

DOI: 10.1039/c7cp08017d

rsc.li/pccp

Introduction

Nitrogen oxides (NO_x) refer to a mixture of compounds containing nitrogen and oxygen. However, this term usually refers to NO, NO₂, and N₂O, due to their larger relative amounts and the fact that the others are unstable and do not appear in the atmosphere.^{1,2} Dinitrogen oxide (N₂O) is a non-toxic gas that mainly comes from the natural microbial denitrification of organic matter.³ Conversely, the source of nitrogen monoxide (NO) and nitrogen dioxide (NO₂) is mainly anthropogenic, being produced in combustion processes, especially at high temperature. Internal combustion engines are their most important sources⁴ along with thermal power stations.⁵ In these processes, excess air used to complete the combustion leads to formation of NO_x in the combustion products. In addition, nitrogen oxides are intermediates in some chemical processes such as the fabrication of nitric acid, paints, nitration of organic chemicals, manufacture of explosives, or as rocket fuels.¹ NO and NO₂ have a high

reactivity with the oxygen from air, being of capital importance in atmospheric chemistry. These gases are the main precursors of tropospheric ozone and other secondary pollutants when they react with oxide volatile organic compounds in the presence of sunlight. They are also responsible for acid rain when combined with water vapor.^{6,7} The release of NO_x from combustion also favors photochemical reactions resulting in the well-known photochemical smog. Additionally, nitrogen oxides are toxic to human inhalation.

The important effects on the environment and human health, along with increasing pollution, leads to the establishment of more restrictive levels of emissions and the need for the appropriate methods to reduce and control the emissions of nitrogen oxides. In order to achieve this aim, there are two main approaches. One focuses on the combustion process itself trying to reduce the amount of NO_x produced. This type of solution achieves ratios of decomposition below 50% in most cases.⁸ The second strategy is based on post-combustion solutions focused on the capture and removal of NO_x after being produced from the combustion products. Among different methods, selective catalytic reduction (SCR) is one of the solutions with higher decomposition ratios while no wastes are produced.^{8,9} The capture and removal of NO and NO₂ is not only an interesting subject in itself but also has importance in carbon dioxide capture and storage processes (CCS). Traces of NO_x and other gases such as sulphur oxides (SO_x) strongly influence the capture and removal of CO₂.^{10–13} As an alternative technology for the removal of NO_x and other pollutants with a better

^a Department of Physical, Chemical and Natural Systems,
University Pablo de Olavide, Sevilla 41013, Spain. E-mail: scalero@upo.es

^b Process and Energy Department, Delft University of Technology,
Leeghwaterstraat 39, 2628CB Delft, The Netherlands

^c Department of Chemical Engineering, Vrije Universiteit Brussel,
Brussels, 1050, Belgium

^d Van't Hoff Institute for Molecular Sciences, University of Amsterdam,
Science Park 904, 1098XH Amsterdam, The Netherlands

† Electronic supplementary information (ESI) available. See DOI: 10.1039/c7cp08017d

efficiency than SCR processes, adsorption in porous materials is an interesting option. With this method, wastes are not produced and the energy requirements are low.^{13–16} The key point for the capture and removal of targeted pollutants is the identification of suitable materials and operation conditions. Zeolites have proved to be efficient molecular sieves for the capture, separation, and purification of mixtures containing small gas molecules.^{13,17,18} These materials exhibit many interesting properties such as a large variety of pore sizes and shapes or high thermal stabilities.¹⁹ Zeolites consist of basic tetrahedral units, in which a central T-atom (usually silicon) is bonded to four oxygen atoms. The basic units are connected generating 3D structures with a huge variety of topologies (*i.e.* cages and/or channels with different directionality) whose effect on the adsorption performance is difficult to screen experimentally. The large amount of available zeolite topologies²⁰ gives to molecular simulations capital importance as a powerful tool to evaluate the performance of porous material and gases at a molecular level with low cost associated.^{21–23}

Simulating systems containing nitrogen monoxide and nitrogen dioxide becomes challenging as these gases co-exist as an equilibrium mixture of their monomer and dimer, depending on the temperature and pressure conditions. The properties of the equilibrium mixtures NO/N₂O₂ and NO₂/N₂O₄ have been extensively studied experimentally and theoretically.^{24–36} For both equilibrium reactions, association is favored at higher values of pressure and low temperature, following Le Chatelier's principle for endothermic dissociation reactions. In the case of the NO/N₂O₂ equilibrium mixture, the fraction of the dimer in the gas phase is very small (less than 3% at temperatures below 180 K and room pressure), and therefore its contribution can be neglected at temperatures above room temperature.^{25,26} The NO₂/N₂O₄ reaction was studied by James and Marshal in the liquid and solid states, reporting equilibrium constants from 77 to 295 K with N₂O₄ fractions larger than 0.99 at temperatures between 250–295 K (strong association in the liquid phase).³³ The gas phase reaction was studied by Chao *et al.*,³² Yoshino *et al.*,³⁰ Verhoek *et al.*,³¹ and Harris and Kenneth,³⁷ among others. These studies show a NO₂ mole fraction in the vapor phase of around 0.9 at 373.15 K and complete dissociation at 413.15 K. The mole fraction of dinitrogen tetroxide rapidly decreases as the pressure decreases or temperature increases. However, dimerization can also occur in the gas phase.³² Thus, *a priori*, dimers must be considered when considering systems containing NO₂ under operation conditions near room pressure and temperature. On the other hand, the properties of gases and liquids adsorbed in narrow pores highly differ from those in the bulk phase. In this regard, the reactive Monte Carlo (RxMC) method, independently developed by Johnson *et al.*³⁸ and Smith and Triska³⁹ for modelling chemical reactions at equilibrium, has been already applied to reactive equilibrium studies,⁴⁰ including (a) simple bulk phase reactions,^{41–44} (b) combined chemical and phase equilibria,^{38,45} and (c) reactions in confined systems,^{41,46–48} among others. In this method, a chemical reaction in a system of interacting molecules is modeled as a Monte Carlo trial move. In one of the initial studies in the literature that

used the RxMC method to determine the composition of a given reaction in a confined geometry, Borówko and Zagórski examined the conversion of a LJ dimerisation reaction within a model pore.⁴⁶ Independently, Turner *et al.* simulated the equilibrium conversion of the ammonia synthesis reaction and the NO dimerisation reaction within a model carbon pore.⁴¹ In these studies, the conversion of the reactions in the pore deviated significantly from the bulk-phase composition, and a strong effect of the pore width was found. Mullen and Maginn recently modeled the xylene isomer mixture in a carbon nanotube, finding a strong dependence between the dominant xylene isomer and the nanotube diameter.⁴⁹ The role of the pore structure was more deeply studied by Hansen *et al.* in zeolites for the propene metathesis reaction system.^{47,48} They also found significant increases in the pore phase conversion compared to the bulk-phase as well as a strong influence of the zeolite topology, temperature and pressure on the pore-phase composition.

Here, we study the effect of confinement on the equilibrium mixture nitrogen dioxide/dinitrogen tetroxide (NO₂/N₂O₄), at different operation conditions of pressure and temperature. We provide insights to understand at a molecular level how the pore structure of the materials modifies the mixture composition by selecting five pure silica zeolites with different topologies: one with cages separated by windows (FAU) and four with intersecting channels and different channel size and directionality (MOR, TON, FER, and MFI). The information given in this paper is organized as follows. Simulation techniques and models for adsorbates and frameworks are detailed in the next section. In Section 3, we discuss the results obtained from the study of the adsorption performance of both species as pure component and binary mixtures, looking at the structural features that differentiate the selected materials. Finally, we provide some concluding remarks in the last section.

Methodology

We use the reactive Monte Carlo method (RxMC) to simulate the equilibrium properties of the reactive system containing nitrogen dioxide and dinitrogen tetroxide, both in the bulk-phase and confined in the FAU, FER, TON, MFI, and MOR zeolites. The RxMC samples the forward and reverse reaction steps in addition to the conventional MC trial moves. The method requires only the input of the full isolated molecule partition functions³⁸ for the reactants and products (or Gibbs-free energies of formation of isolated molecules),³⁹ along with the usual ensemble constants and intermolecular interaction potentials.

The ideal gas partition function for a general case of a non-linear polyatomic molecule is defined⁵⁰ as

$$q(V, T) = \left(\frac{2\pi M k_B T}{h^2} \right)^{3/2} V \cdot \frac{\pi^{1/2}}{\sigma} \left(\frac{T^3}{\Theta_{\text{rot,A}} \Theta_{\text{rot,B}} \Theta_{\text{rot,C}}} \right)^{1/2} \times \left(\prod_{j=1}^{3n-6} \frac{1}{1 - \exp(-\Theta_{\text{vib},j}/T)} \right) \cdot g_{\text{el}} \exp(D_0/k_B T) \quad (1)$$

$\Theta_{\text{rot,A}}$, $\Theta_{\text{rot,B}}$, and $\Theta_{\text{rot,C}}$, are the characteristic rotational constants of the molecule. M denotes the mass of the molecule, $\Theta_{\text{vib},j}$ is the characteristic vibrational temperature corresponding to the normal mode j , D_0 is the atomization energy at 0 K, σ is the rotational symmetry number or external symmetry number of the molecule.⁵⁰ Since only the temperature dependent part of the partition function is needed, dividing eqn (1) by volume, we obtain

$$\hat{q}(T) = \frac{q(V, T)}{V} = \left(\frac{2\pi M k_B T}{h^2} \right)^{3/2} \frac{\pi^{1/2}}{\sigma} \left(\frac{T^3}{\Theta_{\text{rot,A}} \Theta_{\text{rot,B}} \Theta_{\text{rot,C}}} \right)^{1/2} \times \left(\prod_{j=1}^{3n-6} \frac{1}{1 - \exp(-\Theta_{\text{vib},j}/T)} \right) \cdot g_{\text{el}} \exp(D_0/k_B T) \quad (2)$$

This expression can be rearranged and defined in terms of $\hat{q}_0(T)$, an ideal gas partition function (excluding the volume term) in which the ground state energy is zero:

$$\hat{q}(T) = \hat{q}_0(T) \exp(D_0/k_B T) \quad (3)$$

In order to compute the ideal gas partition function, rotational and vibrational constants can be obtained either from *ab initio* quantum calculations or from the experimental data available in the literature, or alternatively from the JANAF thermochemical tables.^{47,50–54} The ideal gas partition functions of nitrogen dioxide and dinitrogen tetroxide used in this study are obtained based on frequency analysis on optimized molecular geometries in Gaussian09 at the mp2 level of theory with the 6-311+G(2d,2p) basis set.⁵⁵ Ideal gas partition functions obtained from *ab initio* calculations are then compared with the ones obtained based on the experimental vibrational and rotational frequencies of nitrogen oxide and nitrogen tetroxide.^{56–61} JANAF thermochemical tables are also used to obtain the ideal gas partition functions.^{50,62} The atomization energy of a molecule D_0 can be determined from the heats of formation at 0 K⁴⁷ and is summarized in Table 1. The temperature dependent parts of the ideal gas partition functions ($\hat{q}_0(T)$) obtained from all three methods are in excellent agreement and are summarized in Table 2. More details about the RxMC method can be found elsewhere.^{39–41,51}

To check the correct reproduction of the single-phase bulk composition of the $\text{NO}_2/\text{N}_2\text{O}_4$ reaction system, simulations in the isobaric–isothermal ensemble have been carried out in combination with reaction sampling (RxMC). The simulations started with 200 NO_2 and 100 N_2O_4 molecules in the system and different conditions of temperature (from 273 to 400 K) and pressure (from 10^1 to 5×10^2 kPa). The Monte Carlo trials performed during the simulations were translation, rotation, reinsertions, volume changes, and reaction sampling.⁶⁴

Table 1 Atomization energies of nitrogen oxide and dinitrogen tetroxide determined based on the heats of formation at 0 K from JANAF tables⁶³

	D_0 [kJ mol ⁻¹]
NO_2	928.47
N_2O_4	1910.10

The results were obtained after running 25 000 equilibration and 250 000 production cycles. The number of Monte Carlo steps per cycle equals the total number of molecules initially in the system. The performance of the $\text{NO}_2/\text{N}_2\text{O}_4$ equilibrium mixture under confinement in porous materials is evaluated by Monte Carlo simulations in the grand-canonical ensemble (GCMC) with and without combination with reaction sampling (RxMC). The extension of the RxMC to the confined system is well established, and this essentially only adds a classical external field to the system.^{38,40,41,48,54} The energy levels of molecules are hardly affected by inter-molecular interactions or this external field at all. A full explanation of the RxMC method and its applications can be found in the new edition of Allen and Tildesley.⁶⁵

In GCMC simulations the temperature and volume are fixed and the bulk-phase reservoir, represented by a fixed chemical potential, is in chemical equilibrium with the pore phase. The chemical potential directly relates to fugacity and fugacity to pressure by means of the fugacity coefficient through the Peng–Robinson equation of state.⁶⁴ For low pressures (ideal gas behavior), the fugacity equals the pressure. The number of cycles used are 50 000 and 500 000 for equilibration and production, respectively. The MC trial moves employed were translation, rotation, reinsertion, swap from the reservoir, and identity change for mixtures. The reaction sampling move was also used in these simulations including the RxMC approach. As in the work of Hansen *et al.*,⁴⁷ the RxMC method in the constant pressure Gibbs ensemble (GE-*NPT*) was also employed along with the reactive GCMC approach to ensure that in our system both approaches for modelling chemical equilibrium led to the same results. The GE-*NPT* simulations started with 350–500 NO_2 molecules in the bulk-phase box and an empty pore phase (zeolite). We used the same number of cycles as in GCMC simulations. The same MC trials are also used, but eliminating identity changes and using transfer trials between simulation boxes (bulk and pore phase, respectively). All simulations are performed using the simulation code RASPA.^{66,67}

The guest–host and guest–guest interactions are described by electrostatic and van der Waals interactions. Electrostatic interactions are considered by using Coulombic potentials and the Ewald summation method.⁶⁴ van der Waals interactions are described by 12-6 Lennard–Jones potentials. A cutoff distance of 14 Å is used, where the interactions are truncated and shifted with tail corrections applied. The nitrogen oxide monomer (NO_2) and dimer (N_2O_4) are modeled according to previous rigid models developed by Bourasseau *et al.*²⁹ Regarding the framework atoms, we use partial charges and Lennard–Jones parameters from the TraPPE-zeo forcefield.⁶⁸ Cross interactions are calculated by the Lorentz–Berthelot mixing rules.⁶⁹ Partial charges and Lennard–Jones parameters used in this work are collected in Table 3.

Five pure-silica zeolites with different geometries and topologies are selected, considering them as rigid frameworks. Despite the well-known fact that the effect of zeolite flexibility could play a role in the diffusion of the molecules in the structure, this effect is usually small in adsorption studies.⁷⁰ Besides, the diffusion

Table 2 Computed temperature dependent part of the ideal gas partition functions (zero ground state energy), as defined in eqn (2) and (3), based on quantum computations using Gaussian09 (mp2/6-311+G(2d,2p)), experimental values from literature and JANAF tables

T (K)	$\hat{q}_0(T) \text{NO}_2/[\text{\AA}^{-3}]$			$\hat{q}_0(T) \text{N}_2\text{O}_4/[\text{\AA}^{-3}]$		
	Gaussian	Literature	JANAF	Gaussian	Literature	JANAF
273.1	1.0757×10^6	1.0611×10^6	1.0636×10^6	1.4386×10^8	1.3349×10^8	1.6113×10^8
298.2	1.4108×10^6	1.3931×10^6	1.3949×10^6	2.3786×10^8	2.1827×10^8	2.6125×10^8
318.1	1.7261×10^6	1.7060×10^6	1.7066×10^6	3.4931×10^8	3.1801×10^8	3.7747×10^8
359.6	2.5396×10^6	2.5160×10^6	2.5149×10^6	7.4668×10^8	6.7010×10^8	7.8575×10^8
374.7	2.8944×10^6	2.8705×10^6	2.8678×10^6	9.7251×10^8	8.6881×10^8	1.0142×10^9
404.0	3.6867×10^6	3.6646×10^6	3.6572×10^6	1.5999×10^9	1.4180×10^9	1.6404×10^9

Table 3 Lennard-Jones parameters and partial charges of the adsorbates and the adsorbents

Atom	ϵ/k_B [K]	σ [Å]	Charge [e^-]
N(NO ₂) ²⁹	50.36	3.24	0.146
O(NO ₂) ²⁹	62.51	2.93	-0.073
N(N ₂ O ₄) ²⁹	50.36	3.24	0.588
O(N ₂ O ₄) ²⁹	62.51	2.93	-0.294
Si (Zeo) ⁶⁸	22.00	2.30	1.50
O (Zeo) ⁶⁸	53.00	3.30	0.75

results achieved using flexibility strongly depend on the model used.⁷¹ A representation of the grid surface energy of the selected materials can be seen in Fig. 1. MOR, TON, FER, and MFI are zeolites with a structure consisting of interconnected channels with different directionality. The crystallographic positions of the atoms of zeolite MOR are taken from the work of Gramlich.⁷² This zeolite is formed by parallel channels in the z -axis with additional adsorption sites in the y -axis. The so-called side pockets are accessible from the main channels only for small molecules.¹⁷ TON zeolite, whose atomic positions are taken from Marler,⁷³ also has a 1D system of channels, but without pockets associated. The channels in MOR are made of 12-member rings, while TON has 10-member rings, resulting in limiting diameters of about 6.5 Å and 5 Å, respectively. FER shows a 2-dimensional intersected system of channels of 4.7 Å (10-member rings in the z -axis) and 3.4 Å (8-member rings in the y -axis).⁷⁴ The 10-member rings also configure the main channels of MFI zeolite (x -axis), which are intersected by zig-zag secondary channels leading to a 3-dimensional system with limiting diameters of around 4.5–4.7 Å.⁷⁵ The last zeolite under study, FAU, has a cubic cell with two types of interconnected cages.⁷⁶ The biggest cages, α -cages, are accessible through a 12-member ring window. The smallest, β -cages or sodalites, are connected by 6-member ring windows but are not accessible for most of the molecules due to the narrow windows that connect them with the α -cages (4-member rings). To comply with the experimental conditions, cavities that are not accessible for the molecules under study need to be blocked.^{77,78} As in a previous work, we use Monte Carlo and Molecular Dynamics simulations to identify these inaccessible cavities.⁷⁹ The first, identifies energetic preferential adsorption sites, while the second informs about the diffusion of the molecules. These sites from which the molecules are unable to escape after 0.15 ns were appropriately blocked. In RASPA, the blockage is implemented using a list of

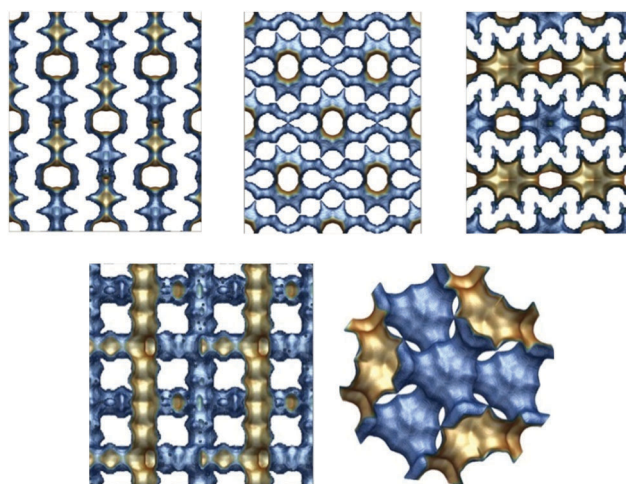


Fig. 1 Energy grid surface of zeolites MOR, TON, and FER (top) and MFI and FAU (down). The accessible surface is colored in brown and the inaccessible surface in blue.

geometric descriptions of the inaccessible volumes that are automatically considered as an overlap in MC simulations. Using this methodology, the sodalites in FAU and the y -axis channels in FER were identified and blocked due to narrow access windows that do not allow diffusion of both molecules under study, considering FER zeolite as the 1-dimensional framework for them. A summary of some other interesting properties of the structures, such as surface area, pore size distributions, and pore volume are computed for later analysis (Table S1 and Fig. S1 in the ESI†).

Results and discussion

Bulk-phase reaction

To validate the molecular models taken from the literature and the partition functions calculated in this work, we carried out RxMC simulations in the isothermal–isobaric (NPT) ensemble for the bulk phase dimer destruction reaction ($\text{N}_2\text{O}_4 \leftrightarrow \text{NO}_2$). The equilibrium constant for the reaction is defined in this work as eqn (4).

$$K_{\text{P[atm]}} = \frac{P_{\text{NO}_2}^2}{P_{\text{N}_2\text{O}_4}} = \frac{(P_{\text{Total}} X_{\text{NO}_2})^2}{P_{\text{Total}} X_{\text{N}_2\text{O}_4}} \quad (4)$$

K_{P} is the equilibrium constant, P_{Total} is the system total pressure, and $P_{i,j}$ and $X_{i,j}$ are the partial pressures and the mole fractions of

Table 4 Comparison of experimental and calculated equilibrium constants for the N_2O_4 – NO_2 system. Our data were obtained at 1 atm

T [K]	K_p [atm]		This work
	Exp. ³⁶	Calc. ³²	
273.10	0.018	0.018	0.019
298.10	0.136	0.146	0.162
318.10	0.628	0.621	0.688
359.60	7.499	7.487	8.239
374.68	16.180	16.111	17.484
403.93	59.430	60.354	63.485

each species respectively. Equilibrium constants for the reaction over a temperature range of 273–404 K, are shown in Table 4, comparing the experimental, calculated, and simulated results. The original experimental values were obtained by Wourtelz,³⁵ Bodenstern and Boës,³⁴ and Verhoek and Daniels.³¹ The values listed in the table were recalculated by Giauque and Kemp.³⁶ Calculated constants were obtained by Chao *et al.* from the derivation of thermodynamic functions³² and our results were obtained in this work at 1 atm of total pressure. The obtained equilibrium constants are in agreement with data from other

authors for the full range of temperatures. Fig. 2 shows the equilibrium mole fraction of N_2O_4 over the studied range of temperatures at pressures from 0.1 to 5 atm. The reference data from the figure were obtained from Chao *et al.*³² for 0.1 and 1 atm and extrapolated to 0.5 and 5 atm using the reported equilibrium constants. In the figure, the simulated results also describe very well the N_2O_4 equilibrium mole fractions in the full range of temperature and pressure. As expected from experimental evidence, high temperatures favor the destruction of the N_2O_4 dimer molecules. Focusing on the results obtained at ambient pressure, the N_2O_4 mole fraction remains above 0.6 up to room temperature. At higher temperatures, the mole fraction strongly decreases up to less than 0.1 at around 360 K, being almost negligible above 370 K. The increase in pressure has the reverse effect, increasing the fraction of the dimer at a fixed temperature. For example, at room temperature the N_2O_4 fraction is increased from *ca.* 0.3 to *ca.* 0.8 from 0.1 to 5 atm, respectively. Information from Fig. 2 is summarized in Table S2 in the ESI.† Having validated the equilibrium compositions in the bulk phase using our simulations, we study the equilibrium reaction in the pore phase.

Pure component and equimolar binary mixture adsorption isotherms from GCMC simulations

Pure component adsorption isotherms and the equimolar binary mixture of NO_2 and N_2O_4 at room temperature are shown in Fig. 3. The reaction trial move is switched off here. We compute these isotherms in hypothetical pure and equimolar mixture compositions to analyze the adsorption performance of each molecule as a previous stage for further discussion of the equilibrium mixtures and reaction themselves. The pure component adsorption isotherms in Fig. 3a show that NO_2 starts to adsorb in the zeolites at 10 kPa, with loadings at an ambient pressure of around 0.5–1 mol kg^{-1} . The lowest loading at this pressure was found for FAU, the zeolite with the largest pore diameter and cavities (see Table S1 and Fig. S1 in the ESI†) in which the NO_2 molecules are less strongly bound due to energy effects.^{80–82} Saturation loadings are not reached at the highest pressure under study (10^3 kPa), showing the uptakes ordered as

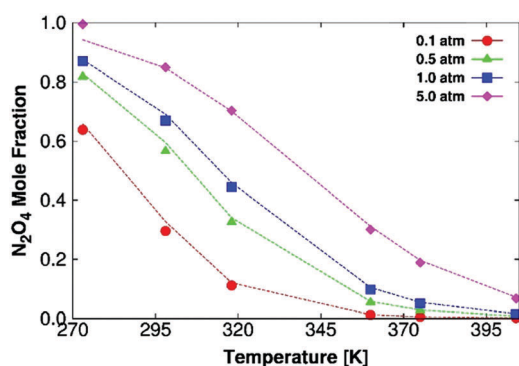


Fig. 2 Mole fraction of N_2O_4 for the bulk phase reaction dimerization over a temperature range of 273–404 K and a pressure range of 0.1–5 atm. Solid symbols depict the results obtained in this work from RxMC simulations in the NPT ensemble and the dashed line shows calculated data from Chao *et al.*³² for direct comparison.

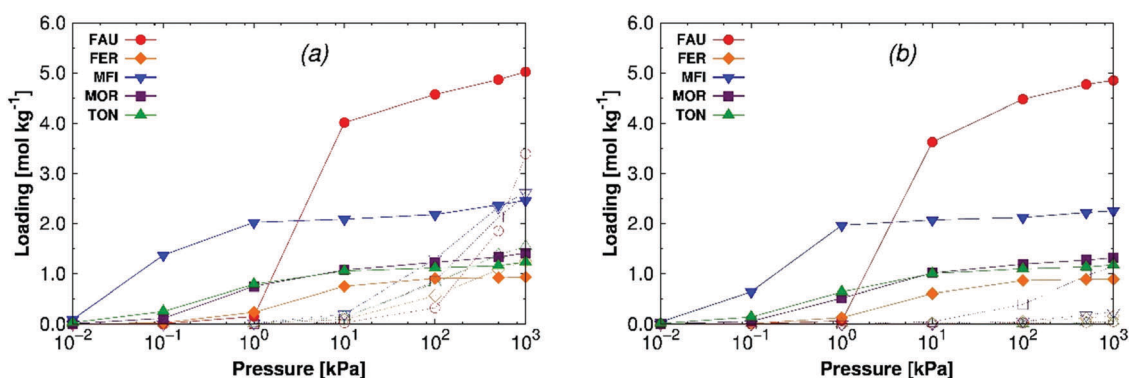


Fig. 3 Calculated pure components (a) and binary equimolar mixture (b) adsorption isotherms of NO_2 (empty symbols) and N_2O_4 (full symbols) at room temperature in FAU (red circles), FER (orange diamonds), MFI (blue down triangles), MOR (purple squares), and TON (green triangles). Reaction trial moves are switched off here.

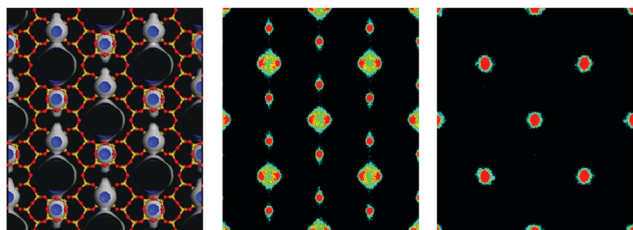


Fig. 4 Average occupation profiles of NO_2 (center) and N_2O_4 (right) in zeolite MOR at 5×10^2 kPa and room temperature. The figure shows the projection of the center of mass of the molecules over the x - y plane. The color gradation (from black to red) indicates the occupation density. To guide the view, a representation of the structure is added (left) where the oxygen atoms are depicted in red and the silica atoms in yellow. A grid surface is also represented where the accessible part is colored in blue and the non-accessible part in gray.

a function of the available pore volume of the zeolites: *ca.* 1.5 mol kg^{-1} (FER and TON), *ca.* 2.5 mol kg^{-1} (MOR and MFI), and *ca.* 3.5 mol kg^{-1} (FAU). Dinitrogen tetroxide adsorption in MFI takes place at 10^{-2} – 10^{-1} kPa, three orders of magnitude of pressure lower than the monomer, and saturation loading (*ca.* 2 mol kg^{-1}) is reached at 1 kPa. In the rest of zeolites adsorption initiates at 10^{-1} – 10^0 kPa and saturation is almost reached at 10 – 10^2 kPa, with loadings of *ca.* 1 – 1.5 mol kg^{-1} (FER, TON and MOR) and 5 mol kg^{-1} (FAU). As for NO_2 , the saturation loadings are ordered as a function of the total pore volume (FAU > MFI > TON > FER), with MOR as an exception. Fig. 4 shows the NO_2 and N_2O_4 average occupation profiles (AOP) in zeolite MOR (more detailed views of the distribution of these molecules can be found in Fig. S2 and S3 in the ESI†). As observed from the figure, while the monomer is absorbed both in the main straight channels and the side pockets, the adsorption of the dimer only takes place in the channels. Part of its pore volume (side pockets) is not accessible for N_2O_4 , explaining why the saturation loading of the dimer in MOR is lower compared to MFI (with a similar pore volume), being closer to the saturation values of TON, which has a similar topology but without side pockets and a lower pore volume than MOR. Adsorption isotherms

from the equimolar binary mixture are shown in Fig. 3b. The adsorption of N_2O_4 is almost unaffected by the presence of NO_2 . Some reduction in loading can be observed at low-medium pressure caused by the fact that the feeder gas stream now contains 50% of each species, but this effect disappears at saturation, with similar loadings as that in the pure component isotherms. In contrast, the adsorption of NO_2 is strongly influenced by the presence of dimers. When N_2O_4 is present in the system, the adsorption of NO_2 drastically decreases to almost negligible values. This behavior occurs in all zeolites except for MOR. In this zeolite, the loading of monomers is reduced about 1 mol kg^{-1} , but with similar N_2O_4 saturation loading, meaning no NO_2 favorable competition for the adsorption sites in the main channels of the structure. As expected from the distribution of molecules as pure components inside this zeolite, the remaining NO_2 adsorption in the equimolar mixture takes place only in the side pockets, where there is no competition with N_2O_4 (see AOP in Fig. S2 and S3 in the ESI†). The presence of these adsorption sites makes a difference in the adsorption performance compared to other structures with very similar topology such as TON or FER, in which the adsorption of monomers is completely displaced from the channels with no alternative adsorption sites.

Bulk-equilibrium binary mixtures

The effect of confinement in the equilibrium mixture containing NO_2 and N_2O_4 is also studied. Adsorption isotherms over an extended range of pressures (10^{-1} – 10^3 kPa) are obtained at room temperature. Isobars at 10^2 and 5×10^2 kPa at temperatures spanning from 260 K and 420 K are also calculated.

Adsorption isotherms. Adsorption results from reactive grand-canonical Monte Carlo simulations for the $\text{N}_2\text{O}_4/\text{NO}_2$ equilibrium mixture at room temperature are shown in Fig. 5. Fig. 5a shows the NO_2 and N_2O_4 adsorption isotherms from equilibrium binary mixtures and Fig. 5b shows the adsorbed mole fraction of N_2O_4 on the zeolites. The composition of the bulk phase at equilibrium was obtained from *NPT* reactive MC simulations and used to fix the GCMC bulk-phase composition (also depicted in Fig. 5b to guide the discussion). Additionally, results obtained

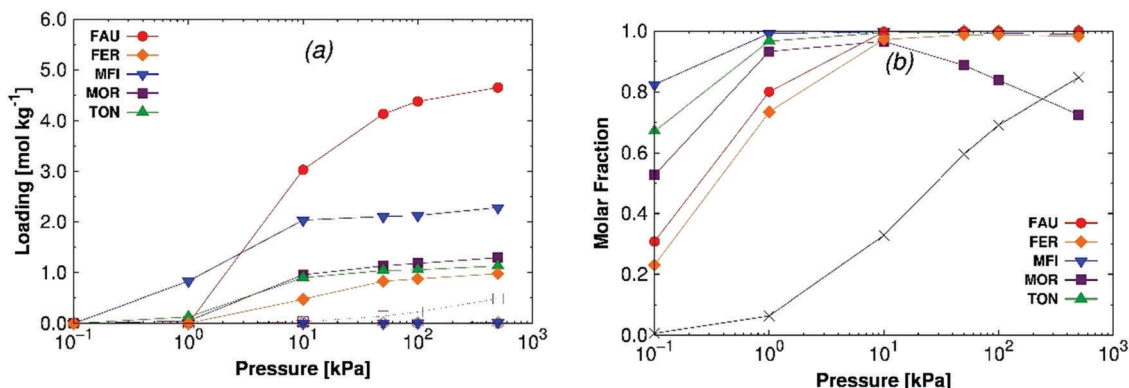


Fig. 5 Calculated binary mixture adsorption isotherms (a), and mole fractions (b) of NO_2 (open symbols) and N_2O_4 (closed symbols) at room temperature in FAU (red circles), FER (orange diamonds), MFI (blue down triangles), MOR (purple squares), and TON (green triangles). To clear the figure and guide the eye in (b), only the N_2O_4 mole fractions are plotted (the sum of both mole fractions is equal to 1) and the bulk mole fractions (obtained from *NPT* reactive simulations) are also added in black. Reaction move is switched on here.

using reactive GCMC are compared to those obtained from reactive constant pressure Gibbs ensemble simulations in Fig. S4 in the ESI.† We compare the results obtained from different methodologies to ensure that the two of them lead to the same results. The agreement using the two approaches allow us to use reactive GCMC simulations for the rest of the study taking advantage of its lower computational cost in comparison with GE-NPT in which both phases need to be simulated at the same time for each simulation.⁴⁷

In Fig. 5a we see a similar behavior as for that observed from the equimolar binary mixture, with some minor differences. At a pressure below 3×10^1 kPa, the mole fraction of N_2O_4 in the bulk is lower than that of NO_2 and the adsorption of N_2O_4 is softly reduced compared to the equimolar binary mixture. The starting adsorption of dimers is displaced one order of magnitude in pressure (from 10^{-1} to 1 kPa) in FER, TOR, and MOR while the loading in MFI is reduced 1 mol kg^{-1} at the same pressure. The adsorption in FAU initiates at the same pressure (1 kPa) but the loading at 10 kPa is also reduced by about 1 mol kg^{-1} . At values of pressure above 3×10^1 kPa, the ratio between the mole fractions of NO_2 and N_2O_4 is reversed and the mole fraction of N_2O_4 becomes larger than that of NO_2 . Saturation loadings are reached in all the zeolites above 10^2 kPa, as described in the binary equimolar mixture. The adsorption of NO_2 at low pressure is almost negligible despite its larger proportions in the bulk phase, and at high pressure the low NO_2 fraction in the bulk phase reduces the number of molecules adsorbed in the side pockets of MOR, the only structure in which there is competition with N_2O_4 in equimolar conditions.

The mole fractions of dinitrogen tetroxide as a function of pressure depicted in Fig. 5b corroborate the fact that confinement goes in favor of dimerization in the full range of pressure. Results at a very low pressure (10^{-1} kPa) should be ignored since the loadings are almost negligible for the two adsorbates. In MFI, an important loading is reached at 1 kPa (*ca.* 1 mol kg^{-1}) the NO_2 adsorbed fraction being almost negligible. From this pressure, the N_2O_4 adsorbed fraction reaches almost 1.0 as NO_2 adsorption is avoided by N_2O_4 molecules in most zeolites. In relation to the influence of zeolite topology on the equilibrium composition of the reaction mixture, MFI shows the strongest influence. This zeolite has one of the narrowest system of channels under study and interconnections where molecules tend to be preferentially absorbed. TON and MOR are the next two structures with the highest N_2O_4 adsorbed fractions at low pressure, being 1D structures with slightly bigger channels than MFI. FAU is the zeolite where both species commensurate the worst. Its high available pore volume and its topology consisting of big cages weaken the confinement of the gas molecules. Finally, the performance of FER can be attributed to the fact that the secondary system of channels of this zeolite is not accessible to the studied molecules and the available pore volume is the smallest among the studied zeolites. Therefore, this structure has the lowest N_2O_4 adsorption at low and high pressure. Focusing on MOR, the adsorption behavior considering the mole fractions of both components as a function of pressure is particularly interesting. At low pressures, the adsorbed fraction

of dimers is larger than the bulk mole fraction, as is the case for the other zeolites. However, once the monomers start entering the side pockets, the trend is inverted. Fig. 5b shows that the adsorbed mole fraction of dimers is lower than that of the bulk fraction at a pressure above 10^2 kPa. This is due to the adsorption of NO_2 molecules in the side pockets of this zeolite, where there is no competition with dimer molecules in spite of its progressive reduction in the bulk phase.

The adsorption selectivity of N_2O_4 over NO_2 is shown in Fig. 6. We defined the adsorption selectivity of component *i* over component *j* (S_{ij}) as $(x_i/y_i)/(x_j/y_j)$ where $x_{i,j}$ are the mole fractions in the adsorbed phase and $y_{i,j}$ the mole fractions in the bulk phase.⁸³ The figure shows that the selectivity up to 10 kPa (before saturation of the pore space) follows the same order as that described in Fig. 5b (MFI > TON > MFI > FAU > FER). This means this is strongly related to the order in which N_2O_4 is adsorbed in the zeolites. At 10 kPa FAU shows a high increase in both loading and selectivity showing the best performance at high pressure. Around 10^1 – 10^2 kPa, N_2O_4 reaches saturation and the loading does not increase despite its bulk fraction increasing for increasing values of pressure, resulting in a reduction of the selectivity but not a significant modification of the adsorbed amount of each component, as can be seen in Fig. 5a. This reduction is particularly important in MOR, the selectivity being inverted towards NO_2 above 10^2 kPa because the main channels are already saturated with N_2O_4 and the amount of NO_2 adsorbed in the side pockets still increases while the NO_2 bulk fraction decreases.

Summarizing, the confinement favors the formation of dimers at any pressure at room temperature, increasing its mole fraction regardless of the bulk phase concentration. However, structural features have to be taken into account carefully as they are able to invert this behavior. This happens in zeolite MOR, where there are sites only accessible for NO_2 which makes them very sensitive to the existence of this species in the gas mixture in contraposition with the rest of the zeolites in which NO_2 can be ignored.

Adsorption isobars. The effect of temperature in the confined equilibrium mixture is analyzed in Fig. 7 at temperatures ranging from 260–400 K. Fig. 7a depicts NO_2 and N_2O_4

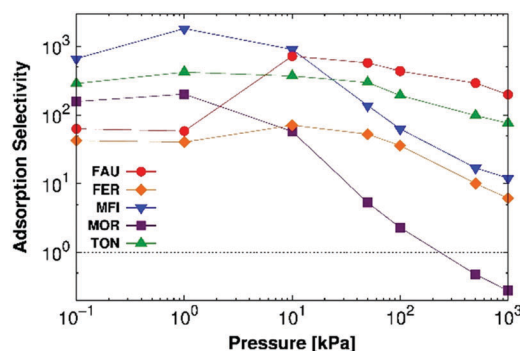


Fig. 6 Adsorption selectivity N_2O_4/NO_2 from the binary equilibrium mixture at room temperature in FAU (red circles), FER (orange diamonds), MFI (blue down triangles), MOR (purple squares), and TON (green triangles). Dotted line in the figure denotes an inversion in the selectivity from a N_2O_4 selective behavior to a NO_2 selective behavior. Reaction move is switched on here.

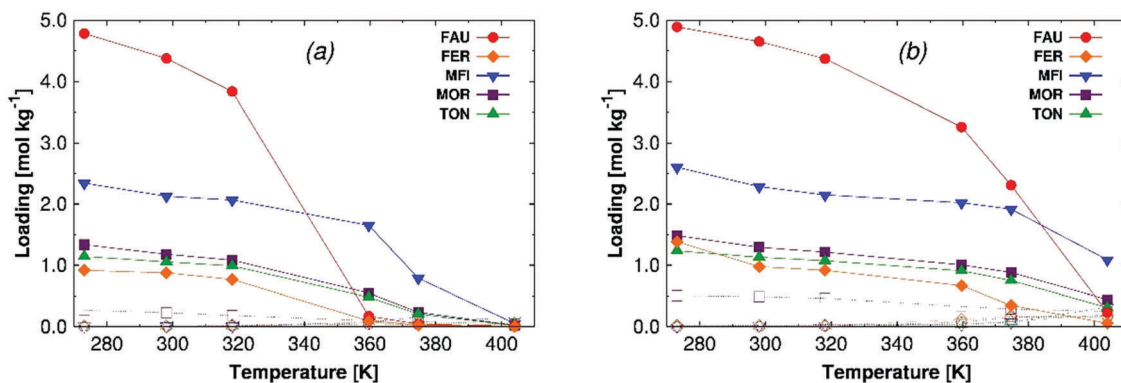


Fig. 7 Calculated binary mixture adsorption isobars of NO₂ (empty symbols) and N₂O₄ (full symbols) at 10² (a) and 5 × 10² kPa (b) in FAU (red circles), FER (orange diamonds), MFI (blue down triangles), MOR (purple squares), and TON (green triangles). Reaction move is switched on here.

adsorbed isobars at room pressure. Dinitrogen tetroxide shows saturation loadings in almost all zeolites below 320 K, with a reduction above this temperature due to a combined effect between the increment in the movement of the particles and the decrease of the N₂O₄ bulk fraction. This reduction is more remarkable in FAU as this zeolite has the highest pore volume and diameter, and N₂O₄ does not fit as tightly as in the other zeolites. Around 370 K only MFI keeps a loading of about a half of its total capacity, while at the highest temperature the loading is almost negligible in all zeolites. The adsorption of NO₂ is very low in all zeolites, even in MOR in which also the side pockets are poorly occupied at temperatures below 320 K (less than 0.5 mol kg⁻¹). No increase in the NO₂ adsorbed amount can be seen when the NO₂ bulk fraction increases with temperature, probably due to a very low pressure preventing NO₂ adsorption. Adsorption isobars at 5 × 10² kPa are depicted in Fig. 7b. At this pressure, the decrease in the adsorbed amount of N₂O₄ at a temperature above 320 K is lesser than that at room pressure, and slightly higher loadings appear at a high temperature. The pressure increase does not affect the NO₂ adsorption at low temperatures in most zeolites due to the low mole fraction in the bulk composition. MOR is the exception since the adsorption of NO₂ in the side pockets is

increased by the pressure increase at low temperatures. In this zeolite, the NO₂ isobar shows a linear behavior as a result of the balanced effect that the temperature exerts on the adsorption performance of this compound. On the one hand, for increasing temperature the bulk fraction of the monomer increases. On the other hand, is the entropic effect and so the adsorption is reduced at higher values of temperature. In the other zeolites, the increment of NO₂ in the bulk fraction with temperature is also responsible of the small rise in its loading at the highest temperature, in contraposition with the decrease of the dimer adsorption.

The adsorbed dinitrogen tetroxide mole fraction from the equilibrium mixture as a function of temperature is depicted in Fig. 8. To see the effect of confinement in the mole fraction and to guide the discussion, the bulk fraction obtained from *NPT* reactive simulations is also depicted in the figure. At ambient pressure (Fig. 8a), the adsorption of N₂O₄ prevails over NO₂ in the full range of temperature, showing a larger fraction of adsorbed dinitrogen tetroxide than that in the bulk. Below 320 K, N₂O₄ fractions near 1 can be observed in all zeolites except MOR, in which they are near 0.8 due to the adsorption of NO₂ in the side pockets. Above this temperature, the reduction in the N₂O₄ loading (Fig. 7a) is responsible for the reduction of

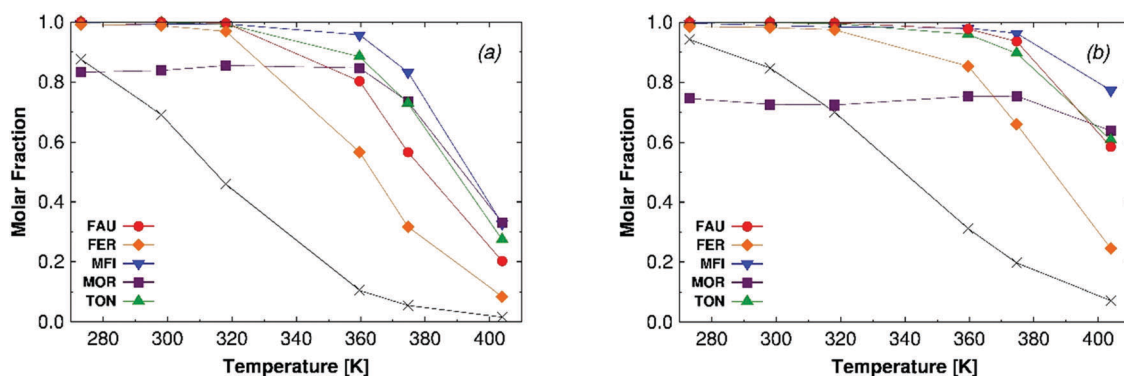


Fig. 8 Calculated binary mixture N₂O₄ adsorbed mole fractions at (a) 10² and (b) 5 × 10² kPa in FAU (red circles), FER (orange diamonds), MFI (blue down triangles), MOR (purple squares), and TON (green triangles). To guide the view, the N₂O₄ bulk mole fraction, obtained from *NPT* reactive simulations, is also added in black. Reaction move is switched on here.

the N_2O_4 adsorbed fraction. For increasing pressure to 5×10^2 kPa, the reduction of N_2O_4 adsorption at 320 K is not so remarkable as that at room pressure because of a stronger N_2O_4 adsorption. The behavior at low pressure is similar for most zeolites, but in this case, MOR shows a reduction in the N_2O_4 adsorbed fraction compared to the bulk. Despite the fact that the adsorption of monomers in MOR takes place at two different pressures in this study, the adsorption is lower at ambient pressure, as this is a low value of pressure for NO_2 to be appropriately adsorbed. At ambient pressure, the adsorbed amount of dimer is larger than expected compared to the bulk phase, with a mole fraction about 20% reduced with respect to other zeolites up to 320 K. In contrast, at the highest value of pressure the adsorbed mole fraction of N_2O_4 is lower than that in the bulk phase up to 320 K, confirming that MOR is very sensitive to the presence of NO_2 , whose initial bulk fraction is lower than 0.10–0.25 between 280–320 K. For increasing temperature, the increase of the monomer mole fraction in combination with the reduction of the total loading adsorbed, reduces and finally eliminates this effect, making this structure more selective to N_2O_4 .

Conclusions

We use molecular simulations to study the effect of the confinement of equilibrium mixtures containing nitrogen dioxide and dinitrogen tetroxide. Models taken from the literature and partition functions calculated in this work were validated by reproducing previously published equilibrium constants and mole fractions of the components in the bulk phase. We verified that the increase of temperature favors the destruction of N_2O_4 , while pressure has the opposite effect. The study of the pure component and equimolar mixtures at room temperature shows that the interaction with all zeolites is stronger for N_2O_4 than for NO_2 , being absorbed by 2–3 orders of magnitude in pressure before and reaching saturation loadings at room pressure. Saturation is not reached in the range of pressure under study for NO_2 in any of the zeolites, and its adsorption was drastically reduced to almost negligible values when introducing N_2O_4 in the system. However, MOR retains a remarkable NO_2 loading due to the existence of special adsorption sites for this molecule where N_2O_4 did not fit. When analyzing the adsorption isotherms and isobars of the reacting mixture in the zeolites, confinement was proved to be responsible for the formation of dimers in the full range of pressure and temperature. Increased density of the adsorbates in the pore phase compared to the bulk, as well as the N_2O_4 selective behavior of the zeolites, are responsible for the N_2O_4 formation. The largest deviations from bulk concentrations were found at low temperatures and high pressures, as the effect of confinement weakens at high temperatures and low pressures due to a decrease in the difference in the adsorption strength of both molecules. Among the studied zeolites, MFI exerts the most noticeable influence in the equilibrium composition since it is a zeolite with one of the narrowest systems of channels accessible to the molecules, closely followed by TON and MOR.

On the other hand, the low available pore volume of FER and the wide size of the cages in FAU, reduce the effect of confinement in these two zeolites. In addition, the selective adsorption sites for NO_2 molecules in MOR strongly modified the general behavior, allowing a high adsorption selectivity towards NO_2 at low temperatures and high pressure. These findings demonstrate that the topological structure of confined systems, such as zeolites, has a crucial influence on the composition of the mixture. The general behavior, N_2O_4 formation in this case, can be modified under certain conditions of pressure and temperature by special structural features such as side-pockets in MOR, as Kim *et al.* have already observed for CO_2/CH_4 separation.⁸⁴ These features must be carefully considered and highlight the need for paying special attention when managing NO_2 adsorption and removal from computational screenings and experimental studies.

Conflicts of interest

There are no conflicts to declare.

Acknowledgements

This work was supported by the MINECO (CTQ2013-48396-P) and by the Andalucía Region (FQM-1851). IMM thanks the Spanish “Ministerio de Educación Cultura y Deporte” for his predoctoral fellowship (FPU13/00281). TJHV acknowledges NWO-CW for a VICI grant. This work was also sponsored by NWO Exacte Wetenschappen (Physical Sciences) for the use of supercomputer facilities, with financial support from the Nederlandse Organisatie voor Wetenschappelijk Onderzoek (Netherlands Organisation for Scientific Research, NWO).

Notes and references

- 1 K. Mollenhauer and H. Tschöke, *Handbook of Diesel Engines*, Springer Berlin Heidelberg, New Delhi, 1st edn, 2010.
- 2 H. Omidvarborna, A. Kumar and D. S. Kim, *Fuel Process. Technol.*, 2015, **140**, 113–118.
- 3 L. Sloss, *Nitrogen Oxides Control Technology Fact Book*, 1992.
- 4 B. Son, W. Yang, P. Breysse, T. Chung and Y. Lee, *Environ. Res.*, 2004, **94**, 291–296.
- 5 A. K. Das, J. D. Wilde, G. J. Heynderickx and G. B. Marin, *AIChE J.*, 2001, **47**, 2831–2844.
- 6 X. L. Zhang, D. O. Hayward, C. Lee and D. M. P. Mingos, *Appl. Catal., B*, 2001, **33**, 137–148.
- 7 V. Sanchez-Escribano, T. Montanari and G. Busca, *Appl. Catal., B*, 2005, **58**, 19–23.
- 8 P. Forzatti and L. Lietti, *Heterog. Chem. Rev.*, 1996, **3**, 33–51.
- 9 M. Shelef, *Chem. Rev.*, 1995, **95**, 209–225.
- 10 E. de Visser, C. Hendriks, M. Barrio, M. J. Mølnvik, G. de Koeijer, S. Liljemark and Y. Le Gallo, *Int. J. Greenhouse Gas Control*, 2008, **2**, 478–484.
- 11 L. F. Ding and A. O. Yazaydin, *J. Phys. Chem. C*, 2012, **116**, 22987–22991.

- 12 J. Yu, Y. Ma and P. B. Balbuena, *Langmuir*, 2012, **28**, 8064–8071.
- 13 I. Matito-Martos, A. Martin-Calvo, J. J. Gutiérrez-Sevillano, M. Haranczyk, M. Doblare, J. B. Parra, C. O. Ania and S. Calero, *Phys. Chem. Chem. Phys.*, 2014, **16**, 19884–19893.
- 14 H. Deng, H. Yi, X. Tang, Q. Yu, P. Ning and L. Yang, *Chem. Eng. J.*, 2012, **188**, 77–85.
- 15 Y. Wang, Z. Huang, Z. Liu and Q. Liu, *Carbon*, 2004, **42**, 445–448.
- 16 Y. Liu, T. M. Bisson, H. Yang and Z. Xu, *Fuel Process. Technol.*, 2010, **91**, 1175–1197.
- 17 E. Garcia-Perez, J. B. Parra, C. O. Ania, A. Garcia-Sanchez, J. M. Van Baten, R. Krishna, D. Dubbeldam and S. Calero, *Adsorpt. Int. Adsorpt. Soc.*, 2007, **13**, 469–476.
- 18 M. P. Bernal, J. Coronas, M. Menendez and J. Santamaria, *AIChE J.*, 2004, **50**, 127–135.
- 19 J. P. Aneousis, *Chem. Eng.*, 1976, **83**, 128.
- 20 C. Baerlocher, L. B. McCusker and D. H. Olson, *Atlas of Zeolite Framework types*, Elsevier, London, 6th edn, 2007.
- 21 W. Sun, L. C. Lin, C. Peng and B. Smit, *AIChE J.*, 2014, **60**, 2314–2323.
- 22 L.-C. Lin, A. H. Berger, R. L. Martin, J. Kim, J. A. Swisher, K. Jariwala, C. H. Rycroft, A. S. Bhowan, M. Deem, M. Haranczyk and B. Smit, *Nat. Mater.*, 2012, **11**, 633–641.
- 23 B. Smit and T. L. M. Maesen, *Chem. Rev.*, 2008, **108**, 4125–4184.
- 24 V. Lachet, B. Creton, T. de Bruin, E. Bourasseau, N. Desbiens, Ø. Wilhelmsen and M. Hammer, *Fluid Phase Equilib.*, 2012, **322–323**, 66–78.
- 25 A. L. Smith and H. L. Johnston, *J. Am. Chem. Soc.*, 1952, **74**, 4696–4698.
- 26 H. J. R. Guedes, PhD thesis, Universidade Nova de Lisboa, Portugal, 1988.
- 27 E. D. Glendening and A. M. Halpern, *J. Chem. Phys.*, 2007, **127**, 164307.
- 28 F. Kohler, *J. Mol. Liq.*, 1995, **67**, 105–123.
- 29 E. Bourasseau, V. Lachet, N. Desbiens, J.-B. Maillet, J.-M. Teuler and P. Ungerer, *J. Phys. Chem. B*, 2008, **112**, 15783–15792.
- 30 K. Yoshino, J. R. Esmond and W. H. Parkinson, *Chem. Phys.*, 1997, **221**, 169–174.
- 31 F. H. Verhoek and F. Daniels, *J. Am. Chem. Soc.*, 1931, **53**, 1250–1263.
- 32 J. Chao, R. C. Wilhoit and B. J. Zwolinski, *Thermochim. Acta*, 1974, **10**, 359–371.
- 33 D. W. James and R. C. Marshall, *J. Phys. Chem.*, 1968, **72**, 2963–2966.
- 34 M. Bodenstein and F. Boës, *Z. Phys. Chem. A*, 1922, **100**, 75.
- 35 E. Wourtsel, *C. R. Acad. Sci. Paris*, 1919, **169**, 1397–1400.
- 36 W. F. Giaouque and J. D. Kemp, *J. Chem. Phys.*, 1938, **6**, 40–51.
- 37 L. Harris and L. K. Churney, *J. Chem. Phys.*, 1967, **47**, 1703–1709.
- 38 J. K. Johnson, A. Z. Panagiotopoulos and K. E. Gubbins, *Mol. Phys.*, 1994, **81**, 717–733.
- 39 W. R. Smith and B. Triska, *J. Chem. Phys.*, 1994, **100**, 3019–3027.
- 40 C. Heath Turner, J. K. Brennan, M. Lísal, W. R. Smith, J. Karl Johnson and K. E. Gubbins, *Mol. Simul.*, 2008, **34**, 119–146.
- 41 H. C. Turner, K. J. Johnson and K. E. Gubbins, *J. Chem. Phys.*, 2001, **114**, 1851–1859.
- 42 L. Pusztai, H. Dominguez and O. A. Pizio, *Rev. Mex. Fis.*, 2003, **49**, 212–218.
- 43 J. Carrero-Mantilla and M. Llano-Restrepo, *Fluid Phase Equilib.*, 2006, **242**, 189–203.
- 44 H. Dominguez and O. A. Pizio, *Phys. A*, 2002, **316**, 65–76.
- 45 M. Lísal, W. R. Smith and I. Nezbeda, *AIChE J.*, 2000, **46**, 866–875.
- 46 M. Borówko and R. Zagórski, *J. Chem. Phys.*, 2001, **114**, 5397–5403.
- 47 N. Hansen, S. Jakobtorweihen and F. J. Keil, *J. Chem. Phys.*, 2005, **122**, 164705.
- 48 S. Jakobtorweihen, N. Hansen and F. J. Keil, *J. Chem. Phys.*, 2006, **125**, 224709.
- 49 R. G. Mullen and E. J. Maginn, *J. Chem. Theory Comput.*, 2017, **13**, 4054–4062.
- 50 D. A. McQuarrie and J. D. Simon, *Physical chemistry: a molecular approach*, University Science Books, Sausalito, California, 1st edn, 1997.
- 51 A. Poursaeidesfahani, R. Hens, A. Rahbari, M. Ramdin, D. Dubbeldam and T. J. H. Vlucht, *J. Chem. Theory Comput.*, 2017, **13**, 4452–4466.
- 52 S. P. Balaji, S. Gangarapu, M. Ramdin, A. Torres-Knoop, H. Zuilhof, E. L. V. Goetheer, D. Dubbeldam and T. J. H. Vlucht, *J. Chem. Theory Comput.*, 2015, **11**, 2661–2669.
- 53 D. R. Stull and H. Prophet, *JANAF thermochemical tables, No. NSRDS-NBS-37*, National Standard Reference Data System, 1971.
- 54 T. W. Rosch and E. J. Maginn, *J. Chem. Theory Comput.*, 2011, **7**, 269–279.
- 55 M. J. Frisch, G. W. Trucks, H. B. Schlegel, G. E. Scuseria, M. A. Robb, J. R. Cheeseman, G. Scalmani, V. Barone, G. A. Petersson, H. Nakatsuji, X. Li, M. Caricato, A. Marenich, J. Bloino, B. G. Janesko, R. Gomperts, B. Mennucci, H. P. Hratchian, J. V. Ortiz, A. F. Izmaylov, J. L. Sonnenberg, D. Williams-Young, F. Ding, F. L. F. Egidi, J. Goings, B. Peng, A. Petrone, T. Henderson, D. Ranasinghe, V. G. Zakrzewski, J. Gao, N. Rega, G. Zheng, W. Liang, M. Hada, M. Ehara, K. Toyota, R. Fukuda, J. Hasegawa, M. Ishida, T. Nakajima, Y. Honda, O. Kitao, H. Nakai, T. Vreven, K. Throssell, J. A. Montgomery, J. E. Peralta, F. Ogliaro, M. Bearpark, J. J. Heyd, E. Brothers, K. N. Kudin, V. N. Staroverov, T. Keith, R. Kobayashi, J. Normand, K. Raghavachari, A. Rendell, J. C. Burant, S. S. Iyengar, J. Tomasi, M. Cossi, J. M. Millam, M. Klene, C. Adamo, R. Cammi, J. W. Ochterski, R. L. Martin, K. Morokuma, O. Farkas, J. B. Foresman and D. J. Fox, *Gaussian 09 Revision C.02*, Gaussian Inc., Wallingford CT, 2016.
- 56 G. Herzberg, *Molecular spectra and molecular structure, electronic spectra and electronic structure of polyatomic molecules*, Van Nostrand, New Jersey, 1966.
- 57 T. Shimanouchi, *J. Phys. Chem. Ref. Data*, 1977, **6**, 993–1102.
- 58 L. M. S. E. P. Krainov and M. A. Kovner, *Vibrational spectra of polyatomic molecules*, New York, 1974.
- 59 J. L. Domenech, A. M. Andrews, S. P. Belov, G. T. Fraser and W. J. Lafferty, *J. Chem. Phys.*, 1994, **100**, 6993.

- 60 M. E. Jacox, *Vibrational and Electronic Energy Levels of Polyatomic Transient Molecules, Journal of Physical and Chemical Reference Data (Book 3)*, American Institute of Physics, 1994.
- 61 A. Stirling, I. Pápai, J. Mink and D. R. Salahub, *J. Chem. Phys.*, 1994, **100**, 2910.
- 62 M. W. Chase, *J. Phys. Chem. Ref. Data*, 1996, **25**, 551–601.
- 63 M. W. Chase, J. L. Curnutt, H. Prophet, R. A. McDonald and A. N. Syverud, *J. Phys. Chem. Ref. Data*, 1975, **4**, 1–176.
- 64 D. Frenkel and B. Smit, *Understanding Molecular Simulations: From Algorithms to Applications*, C. Academic Press, San Diego, CA, 2nd edn, 2002.
- 65 M. P. Allen, D. J. Tildesley and D. J. Tildesley, *Computer Simulation of Liquids*, Oxford University Press, Oxford, 2nd edn, 2017.
- 66 D. Dubbeldam, S. Calero, D. E. Ellis and R. Q. Snurr, *Mol. Simul.*, 2015, **42**, 81–101.
- 67 D. Dubbeldam, A. Torres-Knoop and K. S. Walton, *Mol. Simul.*, 2013, **39**, 1253–1292.
- 68 P. Bai, M. Tsapatsis and J. I. Siepmann, *J. Phys. Chem. C*, 2013, **117**, 24375–24387.
- 69 M. P. Allen and D. J. Tildesley, *Computer Simulation of Liquids*, Oxford Clarendon Press, Oxford, 1987.
- 70 T. J. H. Vlugt and M. Schenk, *J. Phys. Chem. B*, 2002, **106**, 12757–12763.
- 71 A. Garcia-Sanchez, D. Dubbeldam and S. Calero, *J. Phys. Chem. C*, 2010, **114**, 15068–15074.
- 72 V. Gramlich, PhD thesis, ETH, Zürich, Switzerland, 1971.
- 73 B. Marler, *Zeolites*, 1987, **7**, 393–397.
- 74 R. E. Morris, S. J. Weigel, N. J. Henson, L. M. Bull, M. T. Janicke, B. F. Chmelka and A. K. Cheetham, *J. Am. Chem. Soc.*, 1994, **116**, 11849–11855.
- 75 H. van Koningsveld, H. van Bekkum and J. C. Jansen, *Acta Crystallogr., Sect. B: Struct. Sci.*, 1987, **43**, 127–132.
- 76 J. J. A. Hriljac, M. M. M. Eddy, A. K. K. Cheetham, J. A. A. Donohue and G. J. J. Ray, *J. Solid State Chem.*, 1993, **106**, 66–72.
- 77 S. Calero, D. Dubbeldam, R. Krishna, B. Smit, T. J. H. Vlugt, J. F. M. Denayer, J. A. Martens and T. L. M. Maesen, *J. Am. Chem. Soc.*, 2004, **126**, 11377–11386.
- 78 R. Krishna and J. M. van Baten, *Langmuir*, 2010, **26**, 2975–2978.
- 79 I. Matito-Martos, J. Álvarez-Ossorio, J. J. Gutiérrez-Sevillano, M. Doblaré, A. Martín-Calvo and S. Calero, *Phys. Chem. Chem. Phys.*, 2015, **17**, 18121–18130.
- 80 R. Krishna and J. M. van Baten, *Phys. Chem. Chem. Phys.*, 2011, **13**, 10593–10616.
- 81 R. Krishna, B. Smit and S. Calero, *Chem. Soc. Rev.*, 2002, **31**, 185–194.
- 82 A. Torres-Knoop and D. Dubbeldam, *ChemPhysChem*, 2015, **16**, 2046–2067.
- 83 J. Talbot, *AIChE J.*, 1997, **43**, 2471–2478.
- 84 J. Kim, M. Abouelnasr, L.-C. Lin and B. Smit, *J. Am. Chem. Soc.*, 2013, **135**, 7545–7552.